Lab on a Chip

PAPER

View Article Online
View Journal

Check for updates

Cite this: DOI: 10.1039/d2lc00482h

On the robustness of machine learning algorithms toward microfluidic distortions for cell classification *via* on-chip fluorescence microscopy†

Ali Ahmad,[ab] Federico Sala, [cd] Petra Paiè, [d] Alessia Candeo, [c] Sarah D'Annunzio,[e] Alessio Zippo,[e] Carole Frindel,[b] Roberto Osellame, [cd] Francesca Bragheri,[d] Andrea Bassi[cd] and David Rousseau *[a]

Single-cell imaging and sorting are critical technologies in biology and clinical applications. The power of these technologies is increased when combined with microfluidics, fluorescence markers, and machine learning. However, this quest faces several challenges. One of these is the effect of the sample flow velocity on the classification performances. Indeed, cell flow speed affects the quality of image acquisition by increasing motion blur and decreasing the number of acquired frames per sample. We investigate how these visual distortions impact the final classification task in a real-world use-case of cancer cell screening, using a microfluidic platform in combination with light sheet fluorescence microscopy. We demonstrate, by analyzing both simulated and experimental data, that it is possible to achieve high flow speed and high accuracy in single-cell classification. We prove that it is possible to overcome the 3D slice variability of the acquired 3D volumes, by relying on their 2D sum *z*-projection transformation, to reach an efficient real time classification with an accuracy of 99.4% using a convolutional neural network with transfer learning from simulated data. Beyond this specific use-case, we provide a web platform to generate a synthetic dataset and to investigate the effect of flow speed on cell classification for any biological samples and a large variety of fluorescence microscopes (**https://www.creatis.insa-lyon.fr/site7/en/MicroVIP**).

Received 26th May 2022,
Accepted 27th July 2022

DOI: 10.1039/d2lc00482h

rsc.li/loc

Published on 09 August 2022. Downloaded on 9/1/2022 2:18:34 PM.

1 Introduction

Cell cytometry is rapidly evolving thanks to recent technological advances.[1,2] With microfluidics, single cells can now be automatically handled one by one and precisely positioned in front of a detector, opening brand-new possibilities for high-throughput imaging and screening.[3–6] These advances on microfluidics enable analysis of cells based not only on the traditional one-dimensional spectrometric signatures, as in classical flow cytometry,[7,8] but also on their individual spatial characteristics such as shape, texture, size, *etc.*, accessible *via* fluorescence imaging.[9–11] This new approach for cell sorting has also benefited from recent advances in machine and deep learning.[12–15] Demonstrations of cell sorting in microscopy coupled with microfluidics and machine learning have been provided for several research and commercial imaging flow cytometry applications.[16] For instance, it has been used for cell sorting and cancer cell classification based on time-stretch imaging and a deep learning convolutional neural network in ref. 17, for drug-treated and untreated cell classification based on a linear support vector machine (SVM) and convolutional neural networks (CNNs) in ref. 18 and in many other similar cell sorting applications.[13–15,19–21] However in these studies, the impact of sample velocity on cell sorting has not systematically been studied. Flow speed is indeed an important parameter, as it influences both the throughput of the entire process and its performance. Too low a velocity reduces the throughput, while too high a velocity may cause an undesired motion blur effect, as well as a decrease in the number of acquired frames for each cell that may impact the

[a] *Laboratoire Angevin de Recherche en Ingénierie des Systèmes (LARIS), UMR INRAE IRHS, Université d'Angers, 62 Avenue Notre Dame du Lac, 49000 Angers, France. E-mail: david.rousseau@univ-angers.fr*
[b] *Centre de Recherche en Acquisition et Traitement de l'Image pour la Santé (CREATIS), CNRS UMR 5220 – INSERM U1206, Université Lyon 1, Insa de Lyon, Lyon, France*
[c] *Department of Physics, Politecnico di Milano, Piazza Leonardo da Vinci 32, 20133 Milano, Italy*
[d] *Istituto di Fotonica e Nanotecnologie, CNR, Piazza Leonardo da Vinci 32, 20133 Milano, Italy*
[e] *CIBIO, University of Trento, 38123 Trento, Italy*
† Electronic supplementary information (ESI) available. See DOI: **https://doi.org/10.1039/d2lc00482h**

Published on 09 August 2022. Downloaded on 9/1/2022 2:18:34 PM.

cell classification performance. In this article, we propose to investigate the effect of cell flow speed on cell classification *via* on-chip fluorescence microscopy.

As a proof of concept, we selected cancer cell classification based on images acquired on a standard 3D light-sheet fluorescence imaging system coupled with microfluidics.[22,23] This microscopy technique has gained remarkable interest in such applications[24–26] due to its ability to rapidly scan large 3D samples with reduced phototoxicity.[27] We use this system to study the effect of motion blur and of the variable number of image frames per sample. First, we tested this system for a range of cell flow speed values using simulations provided by the open-source MicroVIP simulation platform[28] developed on purpose, and then we compared the results with real datasets. As a disclaimer, let us stress that the instrumentation system is chosen for illustration while the methodology is of generic impact and transposable to more advanced microscopes, higher-throughput microfluidic systems or other biological classification tasks.

This article is organized as follows. The optofluidic configuration and the acquisition of the real images of healthy, cancerous, and metastatic cells with the light sheet microfluidic microscope are first shown. Then, the simulation of the images and the classification methods used in the study are presented. Finally, the impact of cell flow speed on the classification performance of the simulated and real images is discussed.

2 Methods

2.1 Optofluidic setup

The setup consists of an optofluidic device interfaced with a standard inverted microscopy setup, as in ref. 23. The chip contains a single microchannel, used to continuously deliver single cells in suspension to the field of view (FOV) of the microscope, and an embedded cylindrical lens used to generate a plane of light across the channel, corresponding to the microscope objective focal plane. The cells, flowed in the microchannel, cross the plane of light orthogonally during their motion. At the same time, a fluorescence signal is excited by the light-sheet and it is collected by the microscope objective. As the cell flows through the detection plane, the whole volume is collected, plane-by-plane. Since the channel and the lens are realized on the same substrate, no alignment between the two is needed. Furthermore, benefiting from the microfluidic sample delivery, it is possible to perform light sheet fluorescence microscopy (LSFM) of multiple samples in an automated fashion, as in standard cytofluorimetry, guaranteeing a high number of 3D images with a high information content.

A picture and a scheme of the device are reported in Fig. 1. The whole device is realized in fused silica glass, by femtosecond laser micromachining followed by chemical etching.[29] This is a 3D fabrication technique that allows the realization of both the microfluidic channel and micro-optics inside the same glass substrate. The microchannel consists of a top part with a cross-section of 60 × 90 μm^2, corresponding to the detection area, and a bottom part that enlarges in a conical shape. This last design was chosen to match the numerical aperture of the detection objective (60× 1.1 NA water immersion objective) and avoid in this way optical aberrations introduced by the microchannel edges. The chip is realized with an open-channel configuration that is sealed afterwards with a cover glass, 170 μm thick. In this way it is possible to use it in combination with coverslip-corrected detection objectives, to reduce the imaging optical aberrations to the minimum. The cylindrical micro-lens is realized as an air-filled cavity inside the glass substrate, as it has an aspherical engineered profile that generates a light-sheet with a FWHM thickness of 2 μm. The fluidic channel is connected to the external system with some biocompatible PEEK capillaries and to the laser light source with an optical fiber, pigtailed to the device, in front of the micro-lens.

The micro-channel presents a cross-section of approximately 60 × 90 μm^2 that matches the FOV. The channel is imaged using a 60× 1.1 NA water immersion objective (Olympus LUMFLN60XW) so that the FOV is mapped onto the camera sensor with a conversion factor of 0.11 μm per pixel. The sample is flowed at a given speed across the light-sheet, defined as the standard cell flow speed

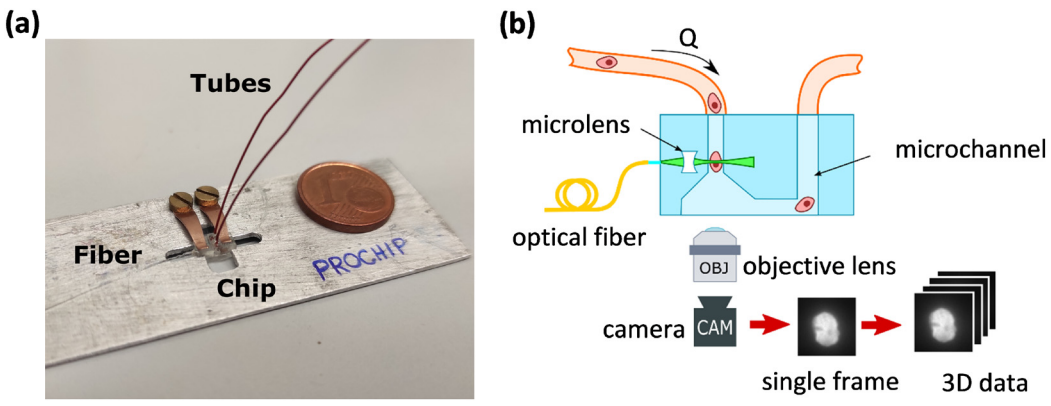

Fig. 1 Optofluidic setup. (a) Original setup image (in comparison with a 1 € cent coin). (b) Scheme of the setup and 3D single cell image acquisition.

This journal is © The Royal Society of Chemistry 2022

Published on 09 August 2022. Downloaded on 9/1/2022 2:18:34 PM.

of 50 nl min^{-1} or the fast cell flow speed of 140 nl min^{-1}, measured and kept constant with an inline flow-meter (MS1 Elveflow), while the detection camera runs in continuous acquisition mode. These flow rates correspond to an average velocity of 0.14 mm s^{-1} and 0.39 mm s^{-1} respectively. The speed is controlled using an external pressure pump (OB1 Elveflow). When a cell passes through the light sheet, custom-made software selects the sub-region of interest and combines the acquired camera frames into a 3D matrix with lateral dimensions of 200 × 200 pixels and a variable number of z-slices that depends on the cell size and cell flow speed. Following this operation mode, the distance between each z-plane is given by

$$d_z = \frac{Q}{A}\frac{1}{\text{frame rate}}, \quad (1)$$

where Q represents the measured flow rate, A is the micro-channel cross-section (5646 μm^2) and the frame rate used is the maximum operable camera acquisition frequency (200 Hz). Following this setup, the cell rate visualization is about 2 cells per s and 5 cells per s for standard and fast cell velocities, respectively. It is important to notice that these throughputs are far from the fastest system found in the state-of-the-art for cell sorting, but comparable with the performances of devices exploiting LSFM and microfluidics to achieve 3D reconstruction.[30,31] Yet, as explained in the next section this range enables a full range of distortion to be investigated due to cell displacement.

2.2 Sample preparation and image acquisition

The cells used to study the impact of cell flow speed on cell classification are hTERT-immortalized human mammary epithelial cells (IMEC WT), xenograft-derived primary tumor cells (XD), and lung metastasis-derived cells (MD). All cell lines were transduced with the PGK-H2B mCherry lentiviral vector (central emission wavelength λ_{em} = 610 nm), and as a result the cells expressed the mCherry H2B recombinant protein in the nucleus. Furthermore, the XD and MD cell lines were obtained by injecting orthotopically IMEC cells overexpressing MYC carrying also the PIK3CA H1047R mutation in NOD/SCID mice as previously described in ref. 32. Before image acquisition, the cells were fixed in 4% PFA for 10 minutes at room temperature. Finally, to avoid cell aggregation and possible clogging of the microfluidic system, ethylenediamine tetra-acetic acid (EDTA) at a concentration of 5 mmol was added to the samples.

The used cells have a typical nucleus diameter of 10–15 μm. Considering these dimensions and a target number of slices per cell ranging from 2 to 25 slices, we chose a flow regime in the interval of 50 to 140 nl min^{-1}, well below the Reynolds number threshold for laminar flow. We limited ourselves to this maximal speed with our system as we are interested in investigating the influence of the number of slices per cell. Two slices is therefore the upper limit

Table 1 Description of the real image datasets used in the study for standard (50 nl min^{-1}) and fast (140 nl min^{-1}) cell velocities: the number of images for each cell type, the range of z-slices ([min max]) and z-spacing (d_z) (in μm)

Cell velocities	# cell images			# z-slices	d_z
	WT	XD	MD	[min max]	(μm)
Standard	1450	1606	2085	[5 25]	0.74
Fast	1380	2236	1890	[2 9]	2.1

independent of the microfluidic-imaging system used. This particular flow regime should ensure the absence of vortexes in the suspension liquid, which means, in first approximation, a rigid translation of the cell along the channel, *i.e.* across the direction perpendicular to the light sheet and to the detection plane. Nevertheless, perturbations in the medium induced by the presence of the lateral walls or by imperfections in the channel cross-section, as well as Brownian motions can still take place. The description of the WT, XD and MD real cell images acquired with both standard and fast speeds is shown in Table 1. From the 3D stacks of images acquired for each cell, 2D z projections corresponding to the sum of each slice of the 3D stacks are produced. In this article we will investigate the classification of the cells both on 3D stacks and 2D projections.

It is important to highlight that fast cell flow speed datasets present a very low z-axis sampling (*i.e.* a small number of z-slices), almost one third of the standard speed counterpart (see Fig. 2). An illustration of the max z and x projections (XY and YZ planes) of the WT cell real images is shown in Fig. 2. Also, as shown in the YZ planes of the cells, it is visible that the level of motion blur increases with the cell speed. Hence, it is interesting to explore the effect of these distortions on the cell classification performance.

2.3 Microfluidic microscopy single cell image simulation

We performed simulations of the possible output of various experimental variables. The light-sheet microscopy image sets can be modeled by

$$I_{LSFM} = \{(P_C * PSF) * \eta(\sigma_m, \theta_m)\} + \beta, \quad (2)$$

where * denotes mathematical convolution, I_{LSFM} is the synthetic 3D microscopy image, P_c is the 3D point cloud of fluorescent markers, and PSF is the experimental point spread function of a light-sheet fluorescence microscope. Microfluidic artifacts were simulated as a convolutional motion blur kernel (η) of size σ_m that depends on the cell flow speed and orientation θ_m. $\beta = \{G, P\}$ is the camera noise module. G is an additive Gaussian noise simulating the thermal and read-out noises and P is a multiplicative Poisson noise simulating the shot noise. Fig. 3 shows a graphical summary of the simulation. The elements of eqn (2) are detailed in the following. This simulation scheme is available as a web-platform (**https://www.creatis.insa-lyon.fr/site7/en/MicroVIP**).

Published on 09 August 2022. Downloaded on 9/1/2022 2:18:34 PM.

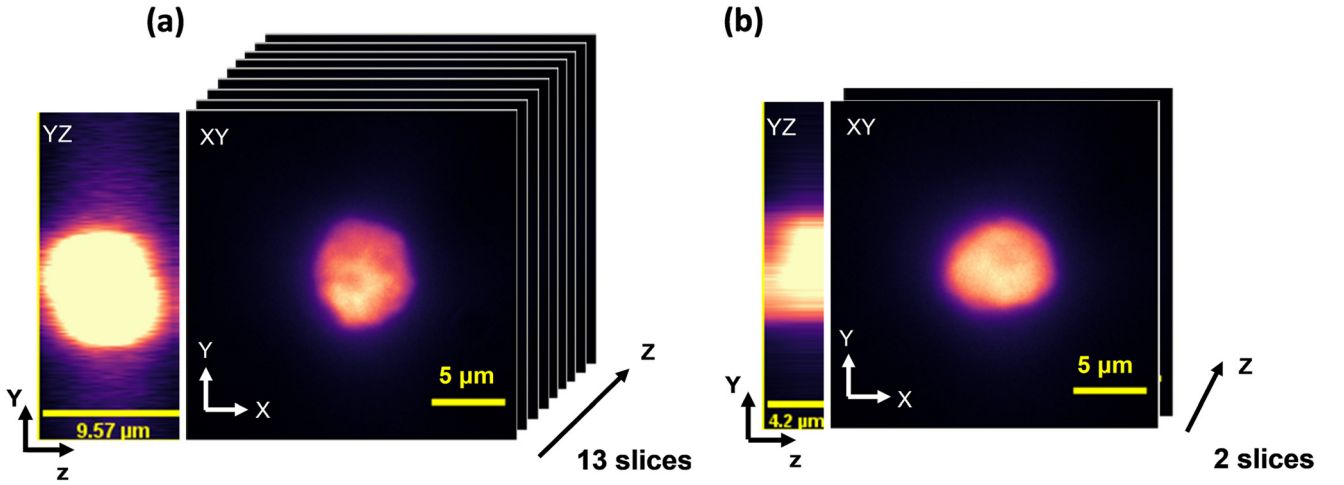

Fig. 2 Illustration of the *XY* and *YZ* planes of the microfluidic light-sheet microscopy images of WT cells. (a) The cell was acquired with a standard cell flow speed of 50 nl min^{-1}. (b) The cell was acquired with a fast cell flow speed of 140 nl min^{-1}. The *XY* size of the images is 200 × 200 pixels (22 × 22 μm) and the *z*-spacing is 0.74 μm for (a) and 2.1 μm for (b). The cells in (a) and (b) are of similar size. The microfluidic effect on the number of acquired *z*-slices and the blurring effect level are visible in the *XY* and *YZ* planes of the (a) and (b) panels.

2.3.1 3D point cloud of fluorescent markers. The 3D point cloud of fluorescent markers was simulated following two steps: (i) modeling 3D chromatin chains and (ii) generation of protein particles. Several types of 3D chromatin chain configuration simulators have been developed in the literature.[33–39] In this work, 3D chromatin chains were modeled according to ref. 36. This method can generate 16 realistic chromatin chains with 100 different configurations for each chain. It is based on a chromosome conformation capture technique (3C-data) and relies on Bayesian inference to derive the 3D architecture of chromatin. The chromatin chains were then interpolated in the *x*, *y*, and *z* directions to simulate several spherical shapes of cells with dimensions ranging from 6 × 6 × 10 to 12 × 12 × 15 μm^3. We used these 3D chains as structures along which the fluorescent markers are distributed. The distance between two successive fluorescent markers along these chains was chosen to follow a uniform (U) distribution. The addition of this last step generates a 3D point cloud of fluorescent markers simulating the protein in the cell volume that is later convolved with the 3D real experimental PSF as shown in Fig. 3(a).

2.3.2 3D experimental point spread function. We used an experimental 3D PSF of a microfluidic light-sheet fluorescence microscope[23] in the simulation of eqn (2). The experimental PSF of 4 × 4 × 9.2 μm^3 was obtained with a water immersion (refractive index n = 1.33) 60× 1.1 NA objective lens using a fluorescent point-like nanoparticle with a central emission wavelength of λ = 580 nm. To determine the lateral and axial resolutions of the microscope, the 3D PSF was fitted with a Gaussian function in the *xy* and *z* directions (see Fig. 3(b)) and the full width at half maximum in the lateral ($FWHM_r$) and axial ($FWHM_z$) directions was estimated as follows

$$FWHM_{r,z} = 2.335\sigma_{r,z}, \quad (3)$$

where $\sigma_{r,z}$ denotes the lateral and axial Gaussian widths fitted with the experimental PSF profiles. The estimated lateral and axial resolutions are found to be $FWHM_r$ = 0.521 μm and $FWHM_z$ = 2.415 μm, respectively. This PSF was convolved with the 3D point cloud to generate the synthetic single-cell image volumes.

2.3.3 Microfluidic artefact simulation. Microfluidic artefacts were simulated as a convolutional motion blur kernel $\eta(\sigma_m, \theta_m)$ applied on the *YZ* planes of the 3D generated images (Fig. 3(c)). The size σ_m of the motion blur depends on the cell flow speed (titQ) inside the micro-channel and the camera characteristics, like the frame rate and shutter speed. The kernel size in the micro-channel space (in μm) is computed as follows

$$\sigma_m = Q \times \text{shutter speed}. \quad (4)$$

The kernel size in the image space (in pixels) could be derived by $\frac{\sigma_m}{d_z}$, where d_z is the *z*-spacing (see eqn (1)). According to this simulation, the motion blur kernel size (σ_m) and the number of *z*-slices of the simulated images are proportional and inversely proportional to the cell flow speed, respectively. In our simulation, the camera frame rate was set to 200 Hz and the shutter speed to $\frac{1}{\text{frame rate}}$, same as those used in the real experiment described in section 2.1. The orientation θ_m of the motion blur kernel was set to zero by considering the cell rotation inside the micro-fluidic device as negligible.

2.3.4 Simulation of camera noise. We have included in the simulation pipeline a camera noise module, with additive thermal and read-out noises modeled as Gaussian noise $G(\mu_n, \sigma_n)$ and shot camera noise taken as multiplicative Poisson noise $P(\lambda_p)$ (Fig. 3(c)). Gaussian noise parameters were computed by fitting the background intensity

 This journal is © The Royal Society of Chemistry 2022

Published on 09 August 2022. Downloaded on 9/1/2022 2:18:34 PM.

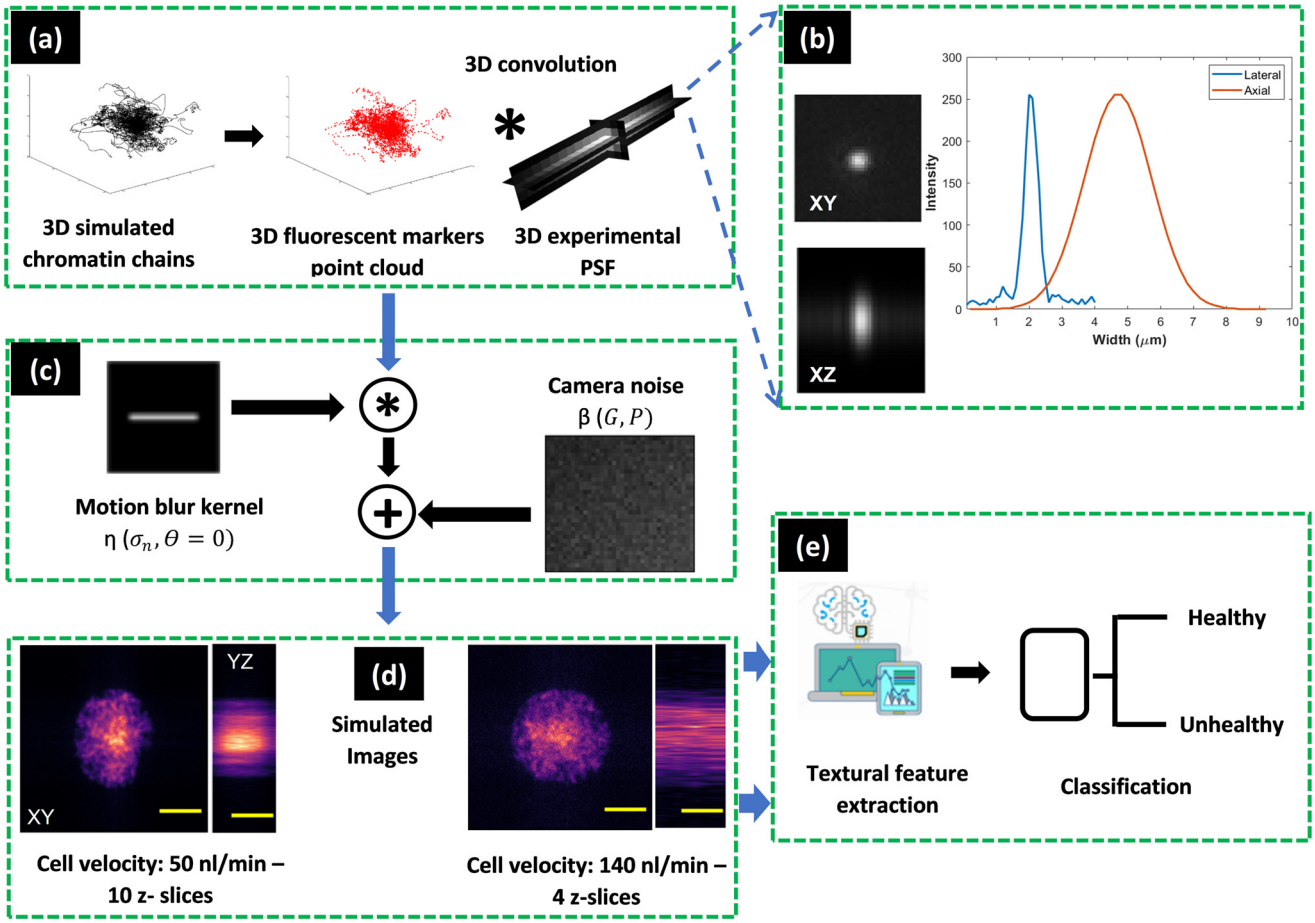

Fig. 3 The overall pipeline of the simulation process. (a) Simulation of 3D chromatin chains with several spatial configurations. The fluorescent markers are generated randomly using a uniform distribution on the chains forming a 3D point cloud. Then, the convolution step is applied with a 3D light-sheet experimental PSF. (b) Lateral and axial profiles of the used experimental PSF. (c) Microfluidic effects simulated as a motion blur kernel are convolved with the 3D synthetic images. A camera noise module was then added to the simulation pipeline (d) to generate the final 3D synthetic light-sheet single-cell images mimicking cells acquired with various cell velocities. 2D images were simulated by applying a sum z-projection transformation to the 3D synthetic microscopy images. Yellow scale bar = 5 μm. (e) Textural features were extracted from 3D and 2D images and were then used to classify healthy/unhealthy cells.

distribution of the real images. The mean μ_n was found to be in the range of (110, 140) gray levels over a full dynamic of 65 536 (16-bit full range) and the standard deviation (σ_n) in the range of (5, 15). The frequency λ_n of the Poisson noise parameter, generally proportional to the number of collected photons, was set empirically to 100.

2.3.5 Simulated single cell images. The results of the simulation scheme of eqn (2) are the 3D light-sheet fluorescence microscopy images (I_{LSFM}) reported in Fig. 3(d). The images were simulated with a size of 200 × 200 pixels corresponding to 22 × 22 μm^2 for an xy pixel resolution of 0.11 μm, while the number of z-slices was computed depending on the sample flow rate ranging from 20 to 140 nl min^{-1}. For this range of cell velocities and cell volumes (from 6 × 6 × 10 to 12 × 12 × 15 μm^3), the retrieved z-spacing d_z values are between 0.29 and 2.1 μm. This leads to simulated 3D images with a z-slice number in the range of [20 50] slices for a cell flow speed of 20 nl min^{-1} and [3 7] slices for 140 nl min^{-1}. This z-slice number is computed as $\left[\frac{\text{min cell size}}{d_z}; \frac{\text{max cell size}}{d_z}\right]$ (*e.g.*, $\left[\frac{6}{0.29} \approx 20; \frac{15}{0.29} \approx 50\right]$). Examples of the simulated images for each cell flow speed are shown in ESI† Fig. S4. Finally, to simulate the 2D images, a z-projection transformation based on the sum of the 3D slices was applied to the 3D simulated microscopy images.

2.3.6 Cell class generation. Diseases like tumors or metastases may be characterized by specific protein spatial redistribution in the chromatin domain.[40,41] For this reason, we based the difference between healthy and unhealthy simulated cells on the density of the fluorescent markers characterising them. Variations in the density were created by changing the parameters of the uniform distribution, such as $U_h(0, 20)$ and $U_{unh}(0, 30)$ for healthy and unhealthy cells, respectively. According to this, we generated a set of 4000 cell images, with 2000 healthy and 2000 unhealthy cells, for each tested cell flow speed ranging from 20 to 140 nl min^{-1}. These generated image classes have been used to study the effects of cell flow speed on cell classification (see Fig. 3(e)).

Published on 09 August 2022. Downloaded on 9/1/2022 2:18:34 PM.

2.4 Classification methods

To study the effects of cell flow speed on healthy and unhealthy cell classification, we propose to perform the classification of 2D/3D simulated and real images on classical textural feature spaces followed by a SVM classifier with a cubic kernel.[42] We also added a deep learning based convolutional neural network (CNN)[43] for the classification of only 2D images. The CNN was not applied on 3D images due to the variability of the number of *z*-slices. The used methods and tested classification strategies are described in the following.

2.4.1 Textural feature extraction and classification. A variety of planar and volumetric textural approach models were proposed in the literature. For illustrative purposes in this study, and without any claim of optimality, we considered the following feature extraction methods:

2.4.1.1 Local binary patterns. We used the mono-scale classical local binary pattern (LBP)[44] for 2D images and the local binary pattern from three orthogonal planes (LBP-TOP)[45] for 3D images (see ESI† Section S1 for a detailed description). We denote the LBP-TOP parameters by LBP-TOP$_{PXY,PXY,PYZ,RX,RY,RZ}$ where the P parameters denote the neighborhood size for each of the three orthogonal planes, while the R parameters denote the radii along the X, Y and Z dimensions of the descriptor. For the present study, the neighborhood size P, for both the LBP and LBP-TOP, was optimized empirically and found to be optimal at P = 16, while the radii were empirically optimized and set to $RX = RY = RZ = 2$. The size of the feature vectors at the output of the LBP-TOP is massive (around 191 000), the reason why a principal component analysis was applied to reduce it to 1000 features, the number of components required to explain at least 99% of variability (see ESI† Fig. S5).

2.4.1.2 Gray level co-occurrence matrix. We also considered the mono-scale classical gray-level co-occurrence matrix (GLCM) method for both 2D and 3D images.[46,47] For 2D images, we computed the GLCMs using the neighbor distance parameter d = 16 pixels as set to the LBP method and used four directions Θ which are: 0°, 45°, 90° and 135°. A set of 14 Haralick coefficients[48] summarizing the GLCM was then computed from 2D microscopy images (see ESI† Section S2). However, for 3D images, we used 13 directions that are defined by the pair (Θ, Φ) with Θ being the angle in the *XY*-plane and Φ being the angle in the *Z*-plane. These 13 directions are: (0°, 0°), (45°, 0°), (90°, 0°), (135°, 0°), (0°, 45°), (0°, 90°), (0°, 135°), (90°, 45°), (90°, 135°), (45°, 45°), (45°, 135°), (135°, 45°) and (135°, 135°). We set also the neighborhood values $d_x = d_y = d_z = 16$ pixels. The Haralick features were then computed for each of the 13 directions and concatenated together for each 3D microscopy image.

2.4.1.3 Scattering transform. In addition, we included a deep feature method based on multi-scale scattering transform (SCATNET) convolution networks applied to images[31,49–51] (see ESI† Section S3 for more details). For the classification of microscopy images, we used the Gabor filter as the mother wavelet with the diffusion transform parameters that were optimized in an empirical way with 3 layers for 4 scales and 8 orientations of the filters (see ESI† Fig. S3). The scattering transform was applied to the 2D images and the three orthogonal planes (*XY*, *YZ*, and *XZ*) of the 3D images computed as the sum *z*, *x*, and *y* projection, respectively.

2.4.1.4 ALL features. As an additional configuration for the cell classification, we combined the mono-scale and multi-scale feature extraction methods by concatenating the features from the LBP, GLCM and SCATNET. We denoted this step by *ALL features* in this article.

This feature extraction and classification pipeline has been applied for each cell flow speed dataset to both simulated and real images. In order to deal with the class imbalance of real images, we used the stratified 10-fold cross-validation method to quantify the classification accuracy of the single cells and to study the effect of the microfluidics. The final accuracy performance was computed as the average of the measured 10-fold accuracies for each method.

2.4.2 Convolutional neural network (CNN) architecture

2.4.2.1 Training from scratch. Beside the classical approaches, we applied a CNN architecture. We used here a VGG16 architecture (ref. 52) for the classification of the 2D images trained with a Tesla V100-DGXS-32GB GPU. Briefly, a VGG16 architecture consists of 13 convolution layers divided to 5 convolution blocks and 3 fully connected layers with (4096, 4096, n_c) neurons, respectively, with n_c being the number of classes equal to 2 for simulated data and 3 for real data. It has a max pooling layer of size 2 × 2 for each convolution block. It uses the softmax function as the output layer and the ReLu activation function is applied to all hidden layers. We trained a VGG16 model for each synthetic and real dataset with the following optimized hyper parameters: filter size = 3 × 3, filter number for the convolution blocks respectively = (64, 128, 256, 512, 512), batch size = 32, number of training epochs = 100, learning rate = 0.0001. In order to provide sufficient amounts of data, a data augmentation step was used on the training sets of simulated and real images. The augmentation operation contained geometrical transformations only such as horizontal and vertical flipping and a random rotational transformation between 0 and 359°. Also, a regularisation step based on early stopping was added during the training to avoid model over-fitting. We used the categorical cross entropy (CCE) as a loss function during model training and it is defined as follows

$$\mathrm{CCE} = -\sum_{c=1}^{J} y_{i,c} \log\left(p_{i,c}\right), \tag{5}$$

where J denotes the number of classes, $y_{i,c}$ is a binary indicator (0 or 1) that indicates whether the class c for the sample i is correct and $p_{i,c}$ denotes the predicted probability for that sample.

 This journal is © The Royal Society of Chemistry 2022

Published on 09 August 2022. Downloaded on 9/1/2022 2:18:34 PM.

2.4.2.2 Transfer learning. Another classification strategy was tested in this study by transferring knowledge from simulated images to real datasets. We applied supervised transfer using classical weight freezing and fine tuning.[53] Models trained on simulated data with cell velocities of 50 nl min^{-1} and 140 nl min^{-1} were used in this process by freezing the first 4 convolution blocks and fine tuning the remaining layers of the VGG architecture with the real dataset of each cell flow speed. In this strategy, we used the same hyper parameters and loss function defined previously.

Similar to what was done for the classical classification pipeline, we used a stratified 10-fold cross-validation method to quantify the classification performance of the 2D images of single cells. In each fold, the datasets were split into training (80%), validation (10%) and test (10%) sets. For each deep learning configuration, the final accuracy was computed as the average of all 10-fold accuracies measured on the test images.

3 Results and discussion

3.1 Results on simulated cells

The accuracy of classification between simulated populations of cells with fluorescent marker density differences as a function of cell flow speed is compared for 2D and 3D microscopy images for various classification methods in Fig. 4. Globally, classification performances are found to be stable even when the cell flow speed increases. This is an interesting result from simulated data, indicating that there is no influence of motion blur and the decreased number of acquired 3D image frames on the cell classification performance. Regarding the question of image dimensions, it should be noted that performances between 2D and 3D spaces vary depending on the used textural features: the shift is important for the GLCM (4(b)) but very limited when the LBP, scattering transform or all feature methods concatenated together are used (4(a), (c) and (d)). Also, it is important to note that the highest classification

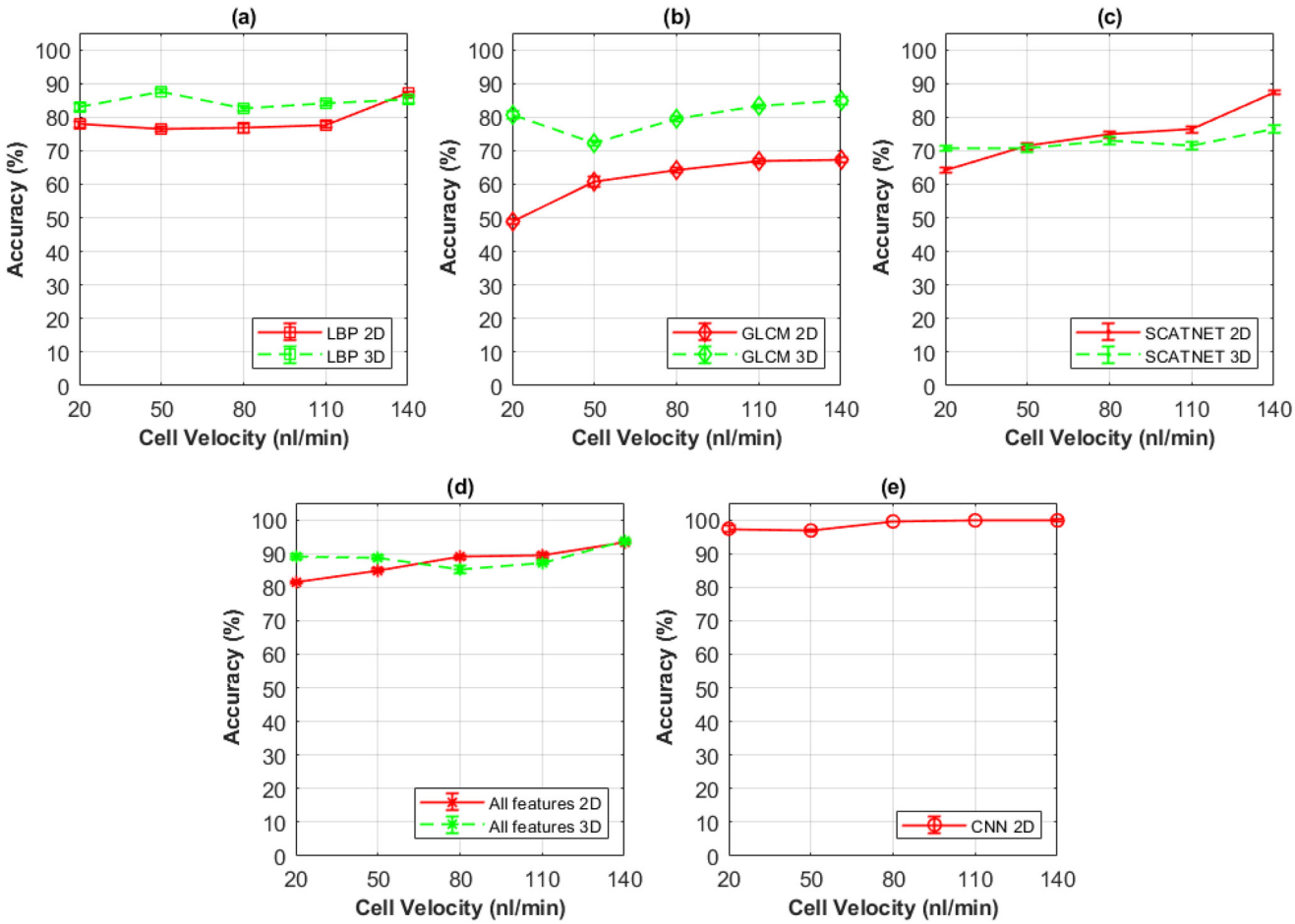

Fig. 4 Classification performances (%) (accuracy) of simulated 2D and 3D microfluidic light-sheet microscopy single-cell images based on density differences of fluorescent markers as a function of the cell flow speed for the tested textural feature methods. (a) LBP, (b) GLCM, (c) scattering transform, (d) all features concatenated together and (e) CNN.

Published on 09 August 2022. Downloaded on 9/1/2022 2:18:34 PM.

performances of 2D and 3D images for classical approaches are of 93%. These are found for the fast cell flow speed (140 nl min^{-1}) when concatenating all textural features (4(d)), the case where the classifier deals with features extracted from different scales of the cells. Finally, deep learning based CNN classification overcomes the classical classification approaches. As shown in the curve of Fig. 4(e), the use of the CNN yields the best classification results of simulated 2D images with an accuracy of 99.8% for the fast cell flow speed. All these results and the limited gap found between 2D and 3D classification performances validate the possibility of using 2D rather than 3D images by selecting an optimal classification strategy, such as the CNN in our case, thus reducing in this way the effect of slice variability and computational time while maintaining an efficient cell classification. These results from simulated data have been validated with the real datasets and the results are discussed in the following.

3.2 Results on real cells

To validate what was found with simulated images, we applied the classification task to real cell images acquired with a cell flow speed of 50 nl min^{-1} as the standard speed (acquisition rate: 2 cells per s) and 140 nl min^{-1} as the fast speed (acquisition rate: 5 cells per s). The classification performances concerning the three classes of real cell images WT, XD, and MD, based on the textural feature spaces and CNN as a function of cell flow speed are presented in Table 2.

The results found are similar to what was found for the simulated images (see Fig. 4). First, for the classical approaches, the classification performances for standard and fast cell velocities are very close, with, globally, a similar to slightly better performance recorded for the fast cell flow speed images as found with the simulation (see also confusion matrices in ESI† Fig. S6–S9). This shows that the degradation of the images caused by the microfluidics has no effect on the image classification when coupling high feature dimensions with machine learning algorithms. Better performance is noticed for the *ALL features* 3D case when the images are acquired with a standard speed (accuracy of 98.1%). However, this performance is found to be very close, or even similar, to the classification performance based on the same textural method when the speed of the cells is faster (accuracy of 96.5%). This result is in line with what was found with the simulation and guarantees the possibility of operating the microfluidic microscopy platform with the highest possible speed maintaining efficient high-throughput cell classification. Second, for the deep learning approaches, the classification performance of cell images acquired with the fast cell flow speed (accuracy of 92.5%) outperforms the accuracy of the classification of images with the standard cell flow speed (accuracy of 84.1%) (see also confusion matrices in ESI† Fig. S10). This result proves again that there is no effect of the microfluidic image degradation on the classification performances. Moreover, the highest classification performance was obtained here with the CNN with the transfer learning classification strategy (CNN with TL in Table 2). Thanks to the simulation pipeline followed in this study, transferring knowledge from realistic simulated data to real datasets leads to an accuracy of classification of 99.4% obtained with the cells acquired with the fast cell flow speed similar to the accuracy obtained with the standard cell flow speed with the same classification conditions (see also confusion matrices in ESI† Fig. S11). These results outperform the classification accuracy obtained with similar applications but with very huge datasets (*e.g.*, accuracy of 94% with a dataset of 10 000 in ref. 54, accuracy of 95% with a dataset of 6700 in ref. 15, accuracy of 92% with a dataset of 240 000 in ref. 18, *etc.*).

Finally, as we look for real time cell acquisition and classification, we compared the feature extraction and classification times of 2D and 3D images for the tested strategies. These computation times are shown in Table 3 and they were obtained with an Intel Core i7-6700HQ CPU@2.60 GHz for the classical feature extraction approaches and with a Tesla V100-DGXS-32GB GPU for CNN deep learning approaches. Although the classification efficiency is high for the 3D images with the classical classification approaches, the results showed a very limited difference in the classification performance between the 2D and 3D images confirming the simulation results (see Fig. 4). However, taking into account the computation time on the one hand, and the difference between the classification performances of 2D and 3D images at a fast speed on the other hand, we found that *ALL features* in 2D lead to the best compromise between the computation time and classification performance for the classical approach. Indeed, the difference in performance between the 2D and 3D images is about ≈2% and the computation time for the 2D images is ≈90% less than that for the 3D images. However, the computation time is still not compatible with a real time application with a fast cell speed given that the needed time to extract and classify 5 cells is about 6.5 seconds, *i.e.* larger than 1 second needed to acquire them. On the other hand, for the CNN with TL approach, where the classification of 2D

Table 2 Real data classification performances (% of accuracy) based on textural feature spaces, CNN and CNN with transfer learning (TL) for both standard (50 nl min^{-1}) and fast (140 nl min^{-1}) cell velocities. Bold-formatted table cells are the highest accuracy values of 2D and 3D for each experiment respectively

	Cell velocities			
	Standard: 50 nl min^{-1}		Fast: 140 nl min^{-1}	
Methods	2D	3D	2D	3D
LBP	90.7 ± 1.4%	95.6 ± 0.8%	87.5 ± 1.3%	91 ± 1.6%
GLCM	79.2 ± 1.8%	84.9 ± 1.7%	82.6 ± 1.3%	85.2 ± 1.5%
SCATNET	91.6 ± 0.9%	96 ± 0.9%	92.5 ± 1.3%	95.2 ± 1.2%
ALL features	94.3 ± 0.9%	**98.1 ± 0.5%**	94.4 ± 0.5%	**96.5 ± 0.4%**
CNN	84.1 ± 3.3%	—	92.5 ± 1.6%	—
CNN with TL	**99.1 ± 0.2%**	—	**99.4 ± 0.5%**	—

This journal is © The Royal Society of Chemistry 2022

Published on 09 August 2022. Downloaded on 9/1/2022 2:18:34 PM.

Table 3 Feature extraction and classification computational time (in seconds) per image for both 2D/3D, standard/fast velocity real images. The bold-formatted table cell is the highest speed value

	Methods								
	2D					3D			
Parameters	LBP	GLCM	SCATNET	*ALL features*	CNN	LBP	GLCM	SCATNET	*ALL features*
Nb of features	243	14	417	674	107×10^6	1000	182	1251	2433
Extraction time	0.34	0.06	0.9	1.3		3.2	8.6	1.6	13.4
Classification time	4.6×10^{-5}	2.3×10^{-5}	6.9×10^{-5}	1×10^{-4}	$\mathbf{1.6 \times 10^{-3}}$	2×10^{-3}	5.7×10^{-5}	2.3×10^{-4}	2×10^{-3}

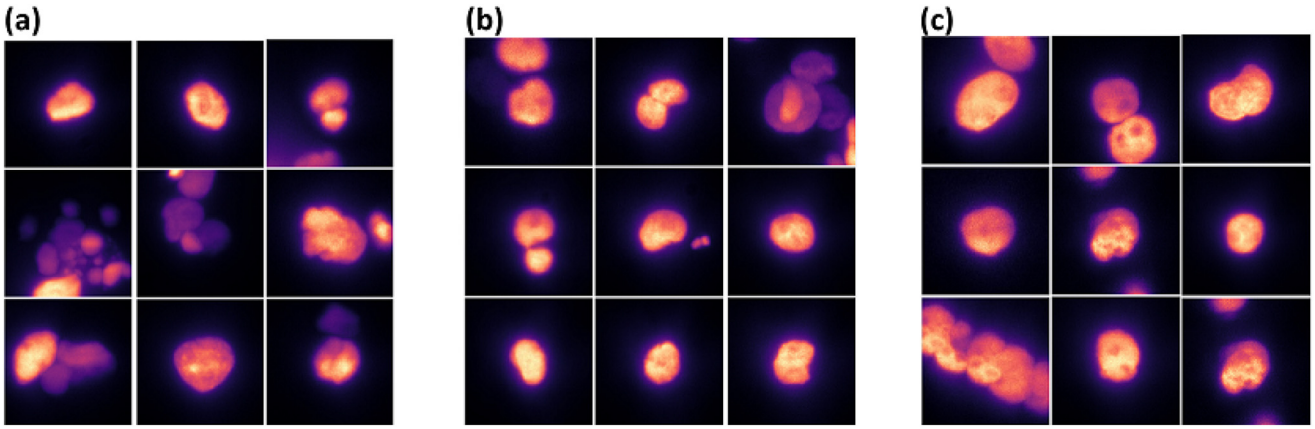

Fig. 5 Illustration of misclassified cell image *XY* planes collected from various classification experiments of Table 2. (a) WT, (b) XD and (c) MD.

images outperforms all the other tested strategies, the classification time of one cell is very fast (1.6×10^{-3}), *i.e.* compatible with an application of real time screening of single cells acquired with a fast speed (time of 8×10^{-3} seconds for the classification of 5 cells less than 1 second the time needed to acquire them with a fast cell flow speed configuration).

As a consequence, this comparison allows us to consider that cell classification based on the 2D CNN with TL method with a fast cell flow speed of 140 nl min^{-1} could be suitable for real time imaging and classification of the cells with no influence of microfluidic noise on the classification efficiency.

3.3 Analysis of misclassified cell images

An important step during our study was to analyze the images of misclassified cells. Fig. 5(a)–(c) show examples of the misclassified images obtained during the experiments shown in Table 2. Most of the misclassified images are found to contain "false cells" such as dust particles, mitotic cells, misaligned regions of interest, regions of interest containing multiple cells, *etc.* These false cells appear to be the main reason for the classification performance drop more than the microfluidic noises. Furthermore, they present challenges in microfluidics and cytometry. Several solutions can be considered to solve this problem. First, an image pre-processing step can be used, such as *z*-directional image regularization to align the image slices, or machine learning-based segmentation to select a single region of interest. However, this solution only solves part of the problem. Another option would be to add a fourth class for the false cell images. This would allow solving the different sources of the false cells, but it could lead to exclusion of a significant number of the imaged cells from the study. For this, other solutions related to the design of microfluidic systems and cell preparation should be investigated to limit these constraints.

4 Conclusion

This study investigated the effect of distortion on images due to cell displacement during image acquisition using fluorescence microscopy coupled to microfluidics for cell classification. We demonstrated through an illustrative use-case that it is possible to increase the cell flow speed up to its highest value without any loss of classification performances, thanks to the adequate simulation and machine learning strategies. Furthermore, we showed that such classification could be done on 2D images instead of 3D images with very limited loss of classification when coupled with classical approaches based on textural features. Also, we demonstrated the advantage of employing the CNN based deep learning classification method with a transfer learning strategy. This led to the highest classification accuracy of 99.4% and computational time compatible with a real time application of cell sorting in microfluidics operated with fast flow velocity.

The work pipeline presented in this study could be easily transferred to any other cell types in the framework of

Published on 09 August 2022. Downloaded on 9/1/2022 2:18:34 PM.

cytometry application. The machine learning algorithms used in this study were trained and fine-tuned to perform on the immortalized cell lines. The same algorithms could be fine-tuned to classify other cell types. In this work, we used synthetic data obtained with the MicroVIP software. This platform allows the simulation of different samples observed with many microscopy systems. In a future perspective, it would be interesting to apply this hybrid approach (synthetic and real data) on other biological samples or use other imaging conditions. In this work we classified images of cells, and stressed that the computation time was compatible with real-time imaging and processing. It would be interesting to translate the obtained results on a high-throughput platform and perform cell sorting based on the results of the machine learning algorithm presented in this study.

Data availability

The codes used for microscopy image simulation and feature extraction are available here: **https://gitlab.in2p3.fr/guillaume.vanel/microvip**. All the images used for this study are available on request from the authors.

Author contributions

Conceptualization: A. A. and D. R.; data curation: A. A.; formal analysis: A. A. and D. R.; methodology: D. R.; software: A. A.; supervision: C. F. and D. R. F. S. fabricated the chip. F. S., P. P. and A. C. performed the measurements. F. B., R. O. and A. B. conceived the microscope on-chip experiments. A. Z. and S. D. produced the cells. Validation: D. R.; visualization: A. A.; writing – original draft: A. A. and D. R. All authors reviewed the manuscript.

Conflicts of interest

There are no conflicts to declare.

Acknowledgements

This work has been supported by project EU H2020 FET Open, PROCHIP, "Chromatin organization PROfiling with high-throughput super-resolution microscopy on a CHIP", grant agreement no. 801336 (**https://pro-chip.eu/**).

Notes and references

1 S. M. Manohar, P. Shah and A. Nair, *Bioanalysis*, 2021, **13**, 181–198.
2 Y. Han, Y. Gu, A. C. Zhang and Y.-H. Lo, *Lab Chip*, 2016, **16**, 4639–4647.
3 L. Ying and Q. Wang, *BMC Biotechnol.*, 2013, **13**, 1–10.
4 Y. Shen, Y. Yalikun and Y. Tanaka, *Sens. Actuators, B*, 2019, **282**, 268–281.
5 N. Nitta, T. Sugimura, A. Isozaki, H. Mikami, K. Hiraki, S. Sakuma, T. Iino, F. Arai, T. Endo and Y. Fujiwaki, *et al.*, *Cell*, 2018, **175**, 266–276.
6 W. E. Khalbuss, L. Pantanowitz and A. V. Parwani, *Pathol. Res. Int.*, 2011, **2011**, 1–10.
7 C. W. Shields IV, C. D. Reyes and G. P. López, *Lab Chip*, 2015, **15**, 1230–1249.
8 R.-J. Yang, L.-M. Fu and H.-H. Hou, *Sens. Actuators, B*, 2018, **266**, 26–45.
9 R. P. Lau, T. H. Kim and J. Rao, *Front. Med.*, 2021, **8**, 1–9.
10 G. Gopakumar, K. H. Babu, D. Mishra, S. S. Gorthi and G. R. S. Subrahmanyam, *J. Opt. Soc. Am. A*, 2017, **34**, 111–121.
11 Y. Gu, A. Chen, X. Zhang, C. Fan, K. Li and J. Shen, *ASP Transactions on Pattern Recognition and Intelligent Systems*, 2021, **1**, 18–27.
12 S. Ota, I. Sato and R. Horisaki, *Microscopy*, 2020, **69**, 61–68.
13 Y. Gu, A. C. Zhang, Y. Han, J. Li, C. Chen and Y.-H. Lo, *Cytometry, Part A*, 2019, **95**, 499–509.
14 M. Sesen and G. Whyte, *Sci. Rep.*, 2020, **10**, 1–14.
15 Y. Li, A. Mahjoubfar, C. L. Chen, K. R. Niazi, L. Pei and B. Jalali, *Sci. Rep.*, 2019, **9**, 1–12.
16 S. Luo, Y. Shi, L. K. Chin, P. E. Hutchinson, Y. Zhang, G. Chierchia, H. Talbot, X. Jiang, T. Bourouina and A.-Q. Liu, *Adv. Intell. Syst.*, 2021, **3**, 2100073.
17 J. B. Ajo-Franklin, S. Dou, N. J. Lindsey, I. Monga, C. Tracy, M. Robertson, V. R. Tribaldos, C. Ulrich, B. Freifeld and T. Daley, *et al.*, *Sci. Rep.*, 2019, **9**, 1–14.
18 H. Kobayashi, C. Lei, Y. Wu, A. Mao, Y. Jiang, B. Guo, Y. Ozeki and K. Goda, *Sci. Rep.*, 2017, **7**, 1–9.
19 I. Constantinou, M. Jendrusch, T. Aspert, F. Görlitz, A. Schulze, G. Charvin and M. Knop, *Micromachines*, 2019, **10**, 311.
20 D. V. Voronin, A. A. Kozlova, R. A. Verkhovskii, A. V. Ermakov, M. A. Makarkin, O. A. Inozemtseva and D. N. Bratashov, *Int. J. Mol. Sci.*, 2020, **21**, 2323.
21 Q. T. Lai, K. C. Lee, A. H. Tang, K. K. Wong, H. K. So and K. K. Tsia, *Opt. Express*, 2016, **24**, 28170–28184.
22 J. Huisken, J. Swoger, F. Del Bene, J. Wittbrodt and E. H. Stelzer, *Science*, 2004, **305**, 1007–1009.
23 F. Sala, M. Castriotta, P. Paiè, A. Farina, S. D'Annunzio, A. Zippo, R. Osellame, F. Bragheri and A. Bassi, *Biomed. Opt. Express*, 2020, **11**, 4397–4407.
24 T. Miura, H. Mikami, A. Isozaki, T. Ito, Y. Ozeki and K. Goda, *Biomed. Opt. Express*, 2018, **9**, 3424–3433.
25 Y.-J. Fan, H.-Y. Hsieh, S.-F. Tsai, C.-H. Wu, C.-M. Lee, Y.-T. Liu, C.-H. Lu, S.-W. Chang and B.-C. Chen, *Lab Chip*, 2021, **21**, 344–354.
26 C. Rasmi, K. Rajan, R. Manjithaya and P. P. Mondal, *et al.*, *CLEO: Applications and Technology*, 2017, p. JW2A-55.
27 P. Paiè, R. Martínez Vázquez, R. Osellame, F. Bragheri and A. Bassi, *Cytometry, Part A*, 2018, **93**, 987–996.
28 A. Ahmad, G. Vanel, S. Camarasu-Pop, A. Bonnet, C. Frindel and D. Rousseau, *SoftwareX*, 2021, **16**, 100854.
29 R. Osellame, H. J. Hoekstra, G. Cerullo and M. Pollnau, *Laser Photonics Rev.*, 2011, **5**, 442–463.
30 A. Isozaki, H. Mikami, H. Tezuka, H. Matsumura, K. Huang, M. Akamine, K. Hiramatsu, T. Iino, T. Ito and H. Karakawa, *et al.*, *Lab Chip*, 2020, **20**, 2263–2273.

 This journal is © The Royal Society of Chemistry 2022

Published on 09 August 2022. Downloaded on 9/1/2022 2:18:34 PM.

31 J. Bruna and S. Mallat, *CVPR 2011*, 2011, pp. 1561–1566.
32 V. Poli, L. Fagnocchi, A. Fasciani, A. Cherubini, S. Mazzoleni, S. Ferrillo, A. Miluzio, G. Gaudioso, V. Vaira and A. Turdo, *et al.*, *Nat. Commun.*, 2018, **9**, 1–16.
33 R. Zhou and Y. Q. Gao, *Int. J. Mol. Sci.*, 2021, **22**, 1328.
34 D. Rico, D. Kent, N. Karataraki, A. Mikulasova, R. Berlinguer-Palmini, B. A. Walker, B. M. Javierre, L. J. Russell and C. A. Brackley, *Genome Res.*, 2022, DOI: **10.1101/gr.276028.121**.
35 A. Buckle, C. A. Brackley, S. Boyle, D. Marenduzzo and N. Gilbert, *Mol. Cell*, 2018, **72**, 786–797.
36 S. Wang, J. Xu and J. Zeng, *Nucleic Acids Res.*, 2015, **43**, e54.
37 P. Szalaj, P. J. Michalski, P. Wróblewski, Z. Tang, M. Kadlof, G. Mazzocco, Y. Ruan and D. Plewczynski, *Nucleic Acids Res.*, 2016, **44**, W288–W293.
38 W. J. Xie, L. Meng, S. Liu, L. Zhang, X. Cai and Y. Q. Gao, *Sci. Rep.*, 2017, **7**, 1–11.
39 S. Carstens, M. Nilges and M. Habeck, *Proc. Natl. Acad. Sci. U. S. A.*, 2020, **117**, 7824–7830.
40 T. J. Stevens, D. Lando, S. Basu, L. P. Atkinson, Y. Cao, S. F. Lee, M. Leeb, K. J. Wohlfahrt, W. Boucher and A. O'Shaughnessy-Kirwan, *et al.*, *Nature*, 2017, **544**, 59–64.
41 S. Kundu, F. Ji, H. Sunwoo, G. Jain, J. T. Lee, R. I. Sadreyev, J. Dekker and R. E. Kingston, *Mol. Cell*, 2017, **65**, 432–446.
42 M. A. Hearst, S. T. Dumais, E. Osuna, J. Platt and B. Scholkopf, *IEEE Intelligent Systems and their applications*, 1998, **13**, 18–28.
43 Y. LeCun, Y. Bengio and G. Hinton, *Nature*, 2015, **521**, 436–444.
44 T. Ojala, M. Pietikäinen and T. Mäenpää, *IEEE Trans. Pattern Anal. Mach. Intell.*, 2002, **24**, 971–987.
45 G. Zhao and M. Pietikainen, *IEEE Trans. Pattern Anal. Mach. Intell.*, 2007, 915–928.
46 E. B. Othmen, M. Sayadi and F. Fniaech, *3rd International Conference on Systems and Control*, 2013, pp. 833–837.
47 A. S. Kurani, D.-H. Xu, J. Furst and D. S. Raicu, *Heart*, 2004, **27**, 25.
48 R. M. Haralick and K. Shanmugam, *et al.*, *IEEE Trans. Syst. Man Cybern. Syst.*, 1973, **3**, 610–621.
49 J. Bruna and S. Mallat, *IEEE Trans. Pattern Anal. Mach. Intell.*, 2013, **35**, 1872–1886.
50 A. Rakotomamonjy, C. Petitjean, M. Salaün and L. Thiberville, *Artif. Intell. Med.*, 2014, **61**, 105–118.
51 P. Rasti, A. Ahmad, S. Samiei, E. Belin and D. Rousseau, *Remote Sens.*, 2019, **11**, 249.
52 K. Simonyan and A. Zisserman, *arXiv*, 2014, preprint, arXiv:1409.1556, DOI: **10.48550/arXiv.1409.1556**.
53 J. Yosinski, J. Clune, Y. Bengio and H. Lipson, *arXiv*, 2014, preprint, arXiv:1411.1792, DOI: **10.48550/arXiv.1411.1792**.
54 Y. Wu, A. Calis, Y. Luo, C. Chen, M. Lutton, Y. Rivenson, X. Lin, H. C. Koydemir, Y. Zhang and H. Wang, *et al.*, *ACS Photonics*, 2018, **5**, 4617–4627.